

Multi-Physics Simulations via Coupled Fourier Neural Operator

Shibo Li^{*†}

*Department of Computer Science
Florida State University*

SHIBOLI@CS.FSU.EDU

Tao Wang^{*}

*Hildebrand Department of Petroleum and Geosystems Engineering
The University of Texas at Austin*

TAO.WANG@UTEXAS.EDU

Yifei Sun

*School of Information
University of Michigan*

YIFEISUN@UMICH.EDU

Hewei Tang

*Hildebrand Department of Petroleum and Geosystems Engineering
The University of Texas at Austin*

HEWEI.TANG@AUSTIN.UTEXAS.EDU

Abstract

Physical simulations are essential tools across critical fields such as mechanical and aerospace engineering, chemistry, meteorology, *etc.*. While neural operators, particularly the Fourier Neural Operator (FNO), have shown promise in predicting simulation results with impressive performance and efficiency, they face limitations when handling real-world scenarios involving coupled multi-physics outputs. Current neural operator methods either overlook the correlations between multiple physical processes or employ simplistic architectures that inadequately capture these relationships. To overcome these challenges, we introduce a novel coupled multi-physics neural operator learning (COMPOL) framework that extends the capabilities of Fourier operator layers to model interactions among multiple physical processes. Our approach implements feature aggregation through recurrent and attention mechanisms, enabling comprehensive modeling of coupled interactions. Our method's core is an innovative system for aggregating latent features from multi-physics processes. These aggregated features serve as enriched information sources for neural operator layers, allowing our framework to capture complex physical relationships accurately. We evaluated our coupled multi-physics neural operator across diverse physical simulation tasks, including biological systems, fluid mechanics, and multiphase flow in porous media. Our proposed model demonstrates a two to three-fold improvement in predictive performance compared to existing approaches.

1. Introduction

Partial differential equations (PDEs) provide the mathematical framework for modeling and predicting physical systems based on fundamental principles of symmetry and conservation laws. (Reed and Simon, 1980; Arnol'd, 2013; Evans, 2022). These equations enable us to represent systems that evolve continuously through space and time, making them essential tools for computational simulation and

. * Equal contribution
. † Corresponding author

forecasting. As the formal language for describing spatiotemporal physical systems, PDEs are central to modeling diverse physical behaviors (Chorin et al., 1990; Bergman, 2011).

Traditional numerical methods, including finite difference, finite element, and finite volume approaches, have long served as standard tools for solving PDEs (Quarteroni et al., 2010; Susanne et al., 1994). However, these conventional approaches face significant limitations due to the curse of dimensionality, as their computational requirements grow exponentially with increasing complexity (LeVeque, 2007; Hughes, 2003). This has driven the development of data-driven alternatives (Kennedy and O’Hagan, 2000; Conti and O’Hagan, 2010; Raissi et al., 2019), particularly neural operators (Kovachki et al., 2023; Lu et al., 2021; Li et al., 2020b,c,a), which offer enhanced computational efficiency. These advanced methods excel by learning the fundamental operators governing PDE behavior, establishing mappings between function spaces to approximate solutions for any input function. This allows them to handle novel scenarios efficiently while avoiding the computational constraints of conventional numerical methods.

While data-driven methods have demonstrated significant success in physical modeling, they encounter substantial challenges when addressing complex multi-physics systems governed by coupled partial differential equations (PDEs) (Keyes et al., 2013; Quarteroni and Quarteroni, 2009). These systems are distinguished by their sophisticated networks of correlated structures and processes, where system-wide behavior emerges from intricate interactions between components (Weinan and Engquist, 2003) rather than from individual elements in isolation. The primary challenge lies in effectively capturing interactions between system components that operate across multiple spatial and temporal scales. This complexity is further amplified by the strong interdependencies between components, which generate nonlinear and often unpredictable outcomes (Cross and Greenside, 2009; Holmes, 2012). Consider the fluid-structure interaction problem (Bazilevs et al., 2013; Bungartz and Schäfer, 2006) as an illustrative example: pressure changes in fluid flow fields directly influence structural deformation, which subsequently modifies the flow field itself, creating a complex feedback loop that must be accurately modeled.

To address the challenges in modeling complex multi-physics systems, we propose COMPOL, a novel coupled operator learning paradigm. Our approach leverages versatile feature aggregation techniques to capture component interactions, encoding them as augmented feature inputs within the operator learning framework. Our work makes three primary contributions:

- We introduce a novel coupled operator architecture that builds upon the Fourier neural operator layer Li et al. (2020a). This paradigm employs feature aggregation techniques to effectively capture component interactions within the operator learning framework, representing a significant advancement in multi-physics modeling capabilities.
- We develop two innovative feature aggregation approaches based on the Fourier neural operator architecture. Our methodology operates within the operator learning paradigm, mapping input functions to output functions through neural operator layers in hidden space (Kovachki et al., 2023). The first approach utilizes recurrent neural networks (RNNs) (Cho et al., 2014), concatenating outputs from previous hidden layers as state inputs. The resulting hidden outputs serve as augmentation features for subsequent layers, enabling the aggregated features to capture interaction information among individual processes effectively. The second approach employs attention mechanisms (Vaswani, 2017), transforming latent features into an alternative space and using multi-head attention to aggregate latent outputs from previous layers. This

enhancement allows for more flexible aggregation of interactions among processes modeled by individual neural operators.

- We evaluate our approach through experiments on several benchmark problems. The results demonstrate that COMPOL achieves superior accuracy in predicting coupled system dynamics while maintaining computational efficiency compared to existing state-of-the-art methods. These findings establish COMPOL as a powerful and flexible framework for simulating coupled and complex multi-physics systems.

2. Background

2.1 Operator Learning

A Partial Differential Equation (PDE) (Evans, 2022) describing a physical system can be expressed mathematically as: $(\mathcal{L}_a(u))(x) = f(x), x \in \Omega; u(x) = 0, x \in \partial\Omega$. In this formulation, $f(x)$ represents the source term, Ω denotes the spatial domain, and $\partial\Omega$ represents its boundary. The solution to the PDE is given by $u(x)$, while L_a represents the differential operator, which may exhibit either linear or nonlinear behavior. Traditional approaches to solving PDEs and conducting physical simulations focus on determining $u(x)$ through analytical or numerical methods, typically involving domain discretization, operator approximation, and solving the resulting system of equations (Brezis, 2011; Quarteroni and Valli, 2008). Data-driven operator learning methods take a fundamentally different approach. These methods aim to construct a parametric mapping ψ_θ between function spaces \mathcal{H} and \mathcal{Y} (e.g., Banach spaces) (Kantorovich and Akilov, 2014). This mapping, denoted as $\psi_\theta : \mathcal{H} \rightarrow \mathcal{Y}$, approximates the inverse operator \mathcal{L}_a^{-1} , which transforms the problem input into its solution $u(x)$. Depending on the specific formulation, the input may consist of the source term $f(x)$, initial condition $u(0)$, or boundary conditions. The training process relies on a dataset \mathcal{D} comprising paired function samples $(\mathbf{f}_n, \mathbf{y}_n)_{n=1}^N$. Each input sample \mathbf{f}_n represents a discretized function $f_n \in \mathcal{H}$, while each output sample \mathbf{y}_n corresponds to the discretized solution $\psi(f_n) \in \mathcal{Y}$. Both input and output functions undergo discretization through value sampling at fixed mesh locations. For example, in a two-dimensional spatial domain $[0, 1] \times [0, 1]$, functions might be sampled on a uniform 64×64 grid. The ultimate goal of operator learning is to determine parameters θ that minimize the empirical loss, thereby approximating the solution operator using the available training data \mathcal{D} .

2.2 Fourier Neural Operator (FNO)

The Fourier Neural Operator (FNO) (Li et al., 2020a) transforms discretized input functions through a two-phase process. First, it uses a feed-forward neural network to map each input element and its sampling location into a higher-dimensional channel space. Second, it applies a Fourier layer that combines linear transformation with nonlinear activation: $v(\mathbf{x}) \leftarrow \sigma(\mathcal{W}v(\mathbf{x}) + \int \kappa(\mathbf{x} - \mathbf{x}')v(\mathbf{x}')d\mathbf{x}')$. The Fourier layer leverages the convolution theorem (Stein and Shakarchi, 2011) to efficiently compute the integral through Fast Fourier Transforms (FFT), reducing computational complexity (Cooley and Tukey, 1965). The architecture completes with multiple stacked Fourier layers and a final feed-forward network that projects features to the output space. Training minimizes an L_p loss function: $\theta^* = \operatorname{argmin}_\theta \frac{1}{N} \sum_{n=1}^N \|\mathbf{y}_n - \psi_{\text{FNO}}(\mathbf{f}_n; \theta)\|_p$ where θ encompasses all model parameters, including the discretized kernel, convolutional layer parameters, and feed-forward network parameters.

2.3 Recurrent Neural Networks (RNNs)

Recurrent Neural Networks (RNNs) (Elman, 1990; Werbos, 1990) are specialized neural architectures designed to process sequential data by maintaining an evolving memory of past information. These networks process sequences $X_T = (x_1, x_2, \dots, x_T)$ through a hidden state h_t that captures information from all preceding elements (x_1, x_2, \dots, x_t) . The core mechanism lies in their state update process at each time step: $h_t = \sigma(W_h h_{t-1} + W_x x_t + b)$, where x_t represents the current input, W_h and W_x denote learnable weight matrices, b represents the bias vector, and $\sigma(\cdot)$ serves as a non-linear activation function. While RNNs effectively process sequential data, they face challenges with longer sequences due to vanishing or exploding gradients during training Bengio et al. (1994). This limitation has led to more sophisticated architectures like Long Short-Term Memory (LSTM) networks (Graves and Graves, 2012) and Gated Recurrent Units (GRUs) (Cho et al., 2014), which introduce specialized mechanisms to better control information flow and preserve long-term dependencies. These innovations have established RNNs as powerful tools for sequence modeling applications, particularly in natural language processing and time series prediction.

2.4 Attention Mechanism

The attention mechanism enables models to process relationships between sequence elements in parallel, regardless of their positions (Bahdanau, 2014; Graves, 2014; Vaswani, 2017). Given an input sequence $X_T \in \mathbb{R}^{T \times d}$ (where T is sequence length and d is embedding dimension), the mechanism transforms the input into three representations through learned weights: $Q = XW_Q$, $K = XW_K$, $V = XW_V$. These query (Q), key (K), and value (V) representations feed into the scaled dot-product attention formula: $A = \text{softmax}(\frac{QK^T}{\sqrt{d_k}})$. The final output $Z = AV$ provides a refined sequence representation where each position incorporates information from all other positions simultaneously. This parallel processing offers significant efficiency advantages over the sequential computation of traditional RNNs.

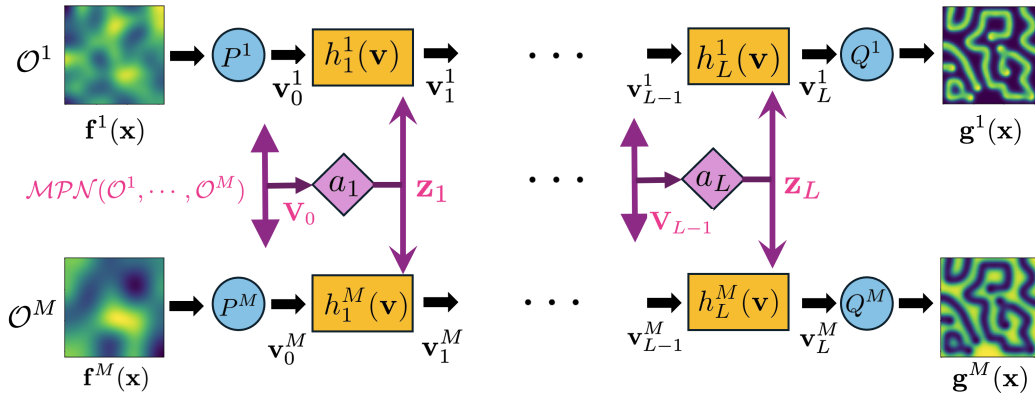


Figure 1: A graphical representation of COMPOL

3. Model

3.1 Multi-Physics Operator Learning

Neural operator learning has demonstrated effectiveness in modeling PDE-governed physical phenomena. However, it faces a fundamental limitation: most approaches assume systems are governed by a single set of PDEs. This simplification fails to capture the reality of physical simulations, where multiple physical processes interact across different scales to produce complex behaviors (Keyes et al., 2013). While current methods attempt to model these interactions through basic techniques like feature concatenation (Wen et al., 2022) and cross-overlaying (Xiao et al., 2023), these approaches prove inadequate for sophisticated simulation scenarios. A coupled multi-physics system is characterized by the interaction and mutual influence of multiple physical processes, governed by different sets of partial differential equations. We can formally define these coupled PDEs as:

$$\begin{cases} (\mathfrak{L}^1(u^1, u^2, \dots, u^M))(x, t) = f^1(x, t) \\ \vdots \\ (\mathfrak{L}^M(u^1, u^2, \dots, u^M))(x, t) = f^M(x, t) \end{cases} \quad (1)$$

Here, \mathfrak{L}^m represents the differential operator for the m -th physical process, with u^m denoting its solution function and f^m representing the source term. The interdependence of differential operators \mathfrak{L}^m on all solution functions u^1, u^2, \dots, u^M highlights the intricate coupling between physical processes. For simplicity, we omit the spatial domain $x \in \Omega_m$ and boundary conditions $u^m(x) = 0, x \in \partial\Omega_m$ for each process $m \in 1 \dots M$. The nonlinear interactions between operators $\mathfrak{L}^1 \dots \mathfrak{L}^M$ generate stiff equation systems requiring sophisticated time integration and fine spatial discretization Oden and Prudhomme (2002); Felippa et al. (2001); Hu et al. (2016). These coupling effects introduce significant numerical challenges that compromise both stability and convergence. While current data-driven approaches attempt to address these challenges through basic techniques, they fail to capture the rich dynamical dependencies between physical processes.

An illustrative example of such coupled systems is the coupled diffusion-reaction process (Grindrod, 1996):

$$\begin{cases} \frac{\partial u}{\partial t} = D_u \Delta u + R_u(u, v), u : \Omega \times (0, T] \rightarrow \mathbb{R} \\ \frac{\partial v}{\partial t} = D_v \Delta v + R_v(u, v), v : \Omega \times (0, T] \rightarrow \mathbb{R}. \end{cases} \quad (2)$$

In this system, u and v represent concentrations of interacting substances over a spatial domain Ω and time interval $(0, T]$. Diffusion coefficients D_u and D_v quantify spatial spread rates, while Laplacian operators Δu and Δv capture spatial variation. The coupled reaction terms $R_u(u, v)$ and $R_v(u, v)$ encapsulate local substance interactions, demonstrating how localized interactions can propagate to influence global system dynamics over time.

3.2 Feature Aggregation for Coupled System

To effectively capture the complex interactions among multiple physical processes in a coupled system, we propose a novel approach that involves computing *feature aggregation states* in the latent space within the framework of neural operator learning. These *feature aggregation states* serve for encoding the intricate relationships and dependencies among the various processes involved. By representing the interactions in a latent space, we can abstract from the raw, high-dimensional, multi-scale data and focus on the essential features and patterns that govern the coupled system’s behavior.

The feature aggregation states act as compact and informative representations that encapsulate the key aspects of the interactions among the physical processes.

As shown in Figure 1., we consider a coupled physical system with M processes, each with corresponding input functions $\mathbf{f}^1, \dots, \mathbf{f}^M$. For each process m , operator \mathcal{O}^m first maps its input function \mathbf{f}^m to a latent representation \mathbf{v}_0^m using a channel-wise linear layer $P^m : \mathbb{R}^{d_m} \rightarrow \mathbb{R}^{d_h}$. Here, d_m denotes the input dimension of process m , and d_h represents the latent dimension. This transformation projects all input functions into a common latent space for unified processing. If each physical process $m \in 1 \dots M$ is modeled individually, without considering the interactions among processes, the operator layer \mathcal{O}^m then applies a neural operator layer $h_1^m : \mathbf{v}_0^m \rightarrow \mathbf{v}_1^m$ for the m -th process. This neural operator layer takes the latent representation \mathbf{v}_0^m as input and transforms it into another latent representation \mathbf{v}_1^m . By stacking L neural operator layers together, each subsequent layer $h_l^m : \mathbf{v}_{l-1}^m \rightarrow \mathbf{v}_l^m$ further transforms the latent function \mathbf{v}_{l-1}^m into \mathbf{v}_l^m for the m -th process. This sequential structure allows for capturing increasingly complex and abstract features of the individual processes. At the end of the stack of neural operator layers, for each process, a channel-wise linear layer $Q^m : \mathbf{v}_L^m \rightarrow \mathbf{g}^m$ is used to map the final latent function \mathbf{v}_L^m back to its corresponding output function \mathbf{g}^m . This final mapping brings the latent representations back to the original function space, allowing for generating the desired output functions. However, this independent modeling approach has a critical limitation: each operator \mathcal{O}^m focuses exclusively on its own process, disregarding the interactions with other processes in the coupled system. This isolation fails to capture the strong correlations and complex dependencies that characterize coupled physical systems.

To address this limitation, we introduce a coupled multi-physics neural operator $\mathcal{MPO}(\mathcal{O}_1, \dots, \mathcal{O}_M)$ to capture the intricate correlations among operators $\mathcal{O}_1, \dots, \mathcal{O}_M$. The core innovation lies in incorporating cross-process information during latent function transformation, enabling comprehensive modeling of process interactions. Our approach centers on feature aggregation states $\{\mathbf{z}_l\}_{l=1}^L$ - shared global latent representations that augment the neural operator layers' inputs. These states facilitate information exchange across processes, allowing the model to capture inter-process dependencies and correlations for a more complete understanding of the coupled system. We implement \mathcal{MPO} using Fourier Neural Operator (FNO) layers, which efficiently capture both local and global information through Fourier transforms. While FNO layers excel at representing complex spatial dependencies in coupled systems, our framework remains adaptable to any operator learning approach that performs sequential latent space transformations.

As the Figure 1. illustrates, our method computes a feature aggregation state \mathbf{z}_l at each neural operator layer h_l^m to capture collective information across all M processes. This state summarizes the cumulative latent information from all processes up to the current layer, defined as:

$$\mathbf{z}_l = \text{Aggregation}_l(\{\{\mathbf{v}_j^m\}_{m=1}^M\}_{j=0}^l)$$

The computed feature aggregation state \mathbf{z}_l then augments the input to each process's next neural operator layer l . Specifically, h_{l+1}^m receives a concatenation of the process-specific latent function \mathbf{v}_l^m and the global aggregation state \mathbf{z}_l . This input allows each layer to process both local process information (\mathbf{v}_l^m) and global cross-process patterns (\mathbf{z}_l), producing an updated latent function \mathbf{v}_{l+1}^m for process m at layer $l + 1$. For implementing the aggregation mechanism, we propose two distinct approaches based on Recurrent Neural Networks (RNNs) and attention mechanisms.

3.3 Recurrent Aggregation State

For notational convenience, let \mathcal{V} represent the complete collection of intermediate latent features across M processes and $L + 1$ layers, where these features are produced by neural operator layers $\{\{h_l^m\}_{m=1}^M\}_{l=0}^L$. Specifically, $\mathcal{V} = \{\{v_l^m\}_{m=1}^M\}_{l=0}^L$. In the one-dimensional case, \mathcal{V} can be viewed as a $(L + 1) \times M \times d_h$ tensor. From this structure, we define \mathbf{V}_l as the $M \times d_h$ matrix obtained by extracting the l -th slice along the first dimension of \mathcal{V} . We further introduce \mathcal{V}_l to represent the sequence of latent functions from layer 0 through layer l , which can be written as $\mathcal{V}_l = \{\mathbf{V}_j\}_{j=0}^l$. Within this notation, two cases are particularly noteworthy: \mathbf{V}_0 represents the collection of latent functions immediately following the channel-wise lifting operation, while \mathbf{V}_L denotes the collection of all latent functions just before the channel-wise projection.

Our first attempt of computing the aggregation state of layer l is with using a recurrent neural network, expressed as:

$$\mathbf{z}_l = \text{RNN}(\mathbf{z}_{l-1}, \mathbf{V}_l).$$

Here, \mathbf{z}_{l-1} represents the aggregation state from the previous layer, and \mathbf{V}_l captures the collective latent transformations across all M processes at layer l . We implement this recurrent mechanism using a Gated Recurrent Unit (GRU) (Cho et al., 2014), defined by:

$$\begin{aligned} \mathbf{q}_l &= \sigma(\mathbf{W}_q \mathbf{V}_l + \mathbf{U}_q \mathbf{z}_{l-1} + \mathbf{b}_q) \\ \mathbf{r}_l &= \sigma(\mathbf{W}_r \mathbf{V}_l + \mathbf{U}_r \mathbf{z}_{l-1} + \mathbf{b}_r) \\ \tilde{\mathbf{z}}_l &= \tanh(\mathbf{W}_z \mathbf{V}_l + \mathbf{U}_z (\mathbf{r}_l \odot \mathbf{z}_{l-1}) + \mathbf{b}_z) \\ \mathbf{z}_l &= \mathbf{q}_l \odot \mathbf{z}_{l-1} + (1 - \mathbf{q}_l) \odot \tilde{\mathbf{z}}_l \end{aligned}$$

where \odot denotes element-wise multiplication. The computation of aggregation state \mathbf{z}_l involves two key intermediary states: the update state \mathbf{q}_l and the reset state \mathbf{r}_l . The update state \mathbf{q}_l functions as a dynamic gate that modulates the balance between preserving information from \mathcal{V}_{l-1} and integrating new information from \mathbf{V}_l , thereby regulating information flow between consecutive layers. The reset state \mathbf{r}_l serves as a filtering mechanism that identifies and removes non-essential historical information, enabling the model to concentrate on the most relevant aspects of the previous aggregation state. The model then computes a candidate state $\tilde{\mathbf{z}}_l$, representing a proposed new aggregation state. This candidate synthesizes the current input \mathbf{V}_l with the selectively filtered historical information $\mathbf{r}_l \odot \mathbf{z}_{l-1}$, offering a novel perspective on the potential aggregation state while maintaining contextually relevant historical information (Jozefowicz et al., 2015; Pascanu, 2013). The final aggregation state \mathbf{z}_l is determined through a strategic combination of the previous state \mathbf{z}_{l-1} and the candidate state $\tilde{\mathbf{z}}_l$, weighted by the update state \mathbf{q}_l . This resulting state encapsulates a carefully calibrated fusion of historical and current information. We demonstrate that this aggregation state effectively captures the intricate interactions up to layer l , enabling the model to harness the complex dynamics inherent in the coupled physical system.

3.4 Attention Aggregation State

Our second approach leverages attention mechanisms to compute the aggregation state \mathbf{z}_l , offering significant advantages over RNN-based methods (Bahdanau, 2014; Vaswani, 2017) in capturing information from \mathcal{V}_l . Unlike the sequential nature of RNNs, attention mechanisms process all elements simultaneously, assigning weights (attention scores) across \mathcal{V}_l . This parallel processing

enables \mathbf{z}_l to dynamically focus on the most significant features within $\mathbf{V}_1, \dots, \mathbf{V}_l$, providing a more versatile and computationally efficient framework for modeling interactions in the latent space of coupled multi-physics systems.

The implementation begins with the application of channel-wise feed-forward neural networks Φ_Q , Φ_K , and Φ_A , which transform \mathcal{V}_l into three distinct representations essential for computing attention scores: query (\mathcal{Q}), key (\mathcal{K}), and value (\mathcal{A}). This transformation can be expressed as:

$$\mathcal{Q} = \Phi_Q(\mathcal{V}_l), \mathcal{K} = \Phi_K(\mathcal{V}_l), \mathcal{A} = \Phi_A(\mathcal{V}_l)$$

The aggregation state at layer l , denoted as \mathbf{z}_l , is then computed through a weighted sum:

$$\mathbf{z}_l = \sum_{k=1}^l \alpha_{lk} \mathbf{A}_k$$

where \mathbf{A}_k represents the k -th slice along the first dimension of \mathcal{A} . The attention weights α_{lk} are determined through a similarity-based computation:

$$\alpha_{lk} = \frac{\exp(s_{lk})}{\sum_{j=1}^l \exp(s_{jk})}, s_{lk} = \frac{\mathbf{Q}_l \mathbf{K}_k^\top}{\sqrt{d_k}}$$

where \mathbf{Q}_l and \mathbf{K}_k represent the l -th and k -th slices along the first dimension of \mathcal{Q} and \mathcal{K} respectively.

This attention mechanism determines feature importance by measuring similarities between \mathcal{Q} and \mathcal{K} representations. The resulting attention scores quantify the relevance of each hidden state \mathbf{V}_j (where $j \in 0, \dots, l$) of \mathcal{V}_l to the current aggregation state \mathbf{z}_l . The final aggregation state is then computed by combining the value representations weighted by these attention scores. This approach enables \mathbf{z}_l to intelligently focus on the most pertinent information, delivering a refined and adaptable method for feature aggregation in coupled multi-physics modeling.

3.5 Training

Given the training data that are simulated or sampled from a coupled multi-physics system, denoted as $\{\{\mathbf{f}_n^m, \mathbf{y}_n^m\}_{n=1}^{N_m}\}_{m=1}^M$, where \mathbf{f}_n^m and \mathbf{y}_n^m represent the n -th input and output functions, respectively, from the m -th process of the coupled system, we optimize our coupled multi-physics neural operator (\mathcal{MPO}) by minimizing the empirical risk,

$$\begin{aligned} \mathcal{L}_{\mathcal{MPO}} &= \mathbb{E}_{m \sim \pi} \mathbb{E}_{f^m \sim \mu^m} \|\mathcal{MPO}(f) - y^m\| \\ &\approx \frac{1}{M} \sum_{m=1}^M \frac{1}{N_m} \sum_{n=1}^{N_m} \|\mathbf{g}_n^m - \mathbf{y}_n^m\|, \end{aligned}$$

where \mathbf{g}_n^m is the prediction of \mathbf{f}_n^m . We can then use any gradient-based optimization method to minimize $\mathcal{L}_{\mathcal{MPO}}$.

4. Related Work

Operator learning represents an innovative approach to surrogate modeling that maps input functions to output functions. Traditional surrogate modeling methods have typically focused on mapping limited sets of system parameters *e.g.*, PDE parameters to output functions *e.g.*, PDE solution

functions, as demonstrated in numerous research works (Higdon et al., 2008; Zhe et al., 2019; Li et al., 2021; Wang et al., 2021; Xing et al., 2021b,a; Li et al., 2022a). Neural operator methods, which leverage neural networks as their foundational architecture, have driven substantial progress in operator learning. The Fourier Neural Operator (FNO) (Li et al., 2020a) emerged alongside a simpler variant, the Low-rank Neural Operator (LNO) (Kovachki et al., 2023), which utilizes a low-rank decomposition of the operator’s kernel to enhance computational efficiency. Building on these innovations, researchers introduced the Graph Neural Operator (GNO) (Li et al., 2020b), which innovatively combines Nystrom approximation with graph neural networks to approximate function convolution. The Multiple Graph Neural Operator (MGNO) (Li et al., 2020c) introduced a multi-scale kernel decomposition approach, achieving linear computational complexity in convolution calculations. Parallel developments included a multiwavelet-based operator learning model (Gupta et al., 2021), which enhanced precision through fine-grained wavelet representations of the operator’s kernel. Another significant contribution emerged with the Deep Operator Net (DeepONet) (Lu et al., 2021), which employs a dual-network architecture combining a branch network for input functions and a trunk network for sampling locations. This architecture was later refined into the POD-DeepONet (Lu et al., 2022), which improved stability and efficiency by replacing the trunk network with POD (or PCA) bases derived from training data. A survey of neural operators is given in (Kovachki et al., 2023). Recent advances in operator learning have focused on developing mesh-agnostic and data-assimilation approaches, representing a significant departure from traditional methods (Yin et al., 2022; Chen et al., 2022; Pilva and Zareei, 2022; Boussif et al., 2022; Esmaeilzadeh et al., 2020). These novel approaches remove the constraint of requiring input and output functions to be sampled on fixed or regular meshes, offering greater flexibility in handling diverse data structures. A key innovation in these methods lies in their reformulation of PDE simulation as an ODE-solving problem. This fundamental shift changes the primary objective from simply predicting solutions based on initial or boundary conditions to capturing the complete dynamic behavior of PDE systems. Training PDE surrogates and neural operators requires extensive high-quality data, which poses a significant challenge due to the resource-intensive nature of physical experiments and sophisticated simulators. To optimize predictive performance while minimizing data collection costs, researchers employ multi-fidelity, multi-resolution modeling Tang et al. (2024, 2023); Li et al. (2023), and active learning approaches (Li et al., 2022b, 2024).

Our approach relates to recent advances in leveraging multi-physics data for neural operator training, though with distinct objectives and methodologies (McCabe et al., 2023; Rahman et al., 2024; Hao et al., 2024). While recent work has focused on developing physics surrogate foundation models by incorporating data from various physics simulations, our research specifically examines the coupled relationships between interaction processes within individual physical systems. The Coupled Multiwavelet Neural Operator (CMWNO) (Xiao et al., 2023) represents the closest parallel to our work, as it similarly aims to model coupled PDEs in complex systems with multiple physical processes. CMWNO employs a specialized approach, decoupling the integral kernel during multi-wavelet decomposition and reconstruction procedures in the Wavelet space. However, this method faces several limitations: it requires particular structures and fixed function decomposition schemes, and its simple cross-over model structure presents challenges for systems with more than two processes. Additionally, CMWNO sometimes struggles to capture complex correlations among different processes effectively. Our proposed method builds upon FNO layers while offering greater flexibility and adaptability. A key advantage of our approach lies in its extensibility - it can be integrated with any neural operator learning framework that conducts layer-wise functional transformations.

Furthermore, our innovative aggregation method readily accommodates any number of physical processes, making it particularly valuable for modeling complex, multi-process systems.

Method	<i>Lotka-Volterra</i>	<i>Coupled-Burgers</i>	<i>Grey-Scott</i>	<i>Multiphase Flow</i>
FNO _c	0.2525 ± 0.0171	4.074e-4 ± 2.428e-5	0.0122 ± 0.0004	0.0204 ± 0.0022
CMWNO	0.2486 ± 0.0359	0.0517 ± 0.0039	-	-
COMPOL-RNN	0.1436 ± 0.0109	2.252e-5 ± 9.531e-7	0.0053 ± 0.0001	0.0186 ± 0.0062
COMPOL-ATN	0.1285 ± 0.0061	1.490e-4 ± 6.426e-6	0.0079 ± 0.0002	0.0159 ± 0.0011
COMPOL-MH-ATN	0.1247 ± 0.0067	1.358e-4 ± 3.546e-6	0.0066 ± 0.0001	0.0137 ± 0.0010

Table 1: Prediction accuracy evaluated using relative L_2 error on four benchmark datasets with 256 training examples. Results show averages from five independent runs to ensure statistical reliability.

5. Experiment

We conducted a comprehensive evaluation of our proposed framework’s performance in predicting solution fields for coupled multi-physics systems, focusing on several benchmark partial differential equations (PDEs) from computational physics. The evaluation encompasses three key equations: the 1-D Lotka-Volterra equations (Murray, 2007), 1-D coupled Burgers’ equations (Larsson and Thomée, 2003), 2-D Gray-Scott equations (Pearson, 1993) and a multiphase flow problem with CO_2 and water in the context of geological storage of CO_2 (Bear and Cheng, 2010; Hashemi et al., 2021; Abou-Kassem et al., 2013). These equations were selected for their diverse characteristics and widespread applications across scientific and engineering domains. To establish a robust training dataset, we employed numerical solvers with multi-mesh discretization. The 1-D experiments utilized a mesh size of 256, while the 2-D experiments employed a 64x64 mesh configuration. We investigated the framework’s performance under varying data availability conditions by conducting experiments with two distinct training set sizes: 256 and 512 examples. Additionally, we generated a separate test set of 200 examples using identical mesh sizes to assess the models’ generalization capabilities effectively. For experimental clarity and computational efficiency, we focused our evaluation on coupled multi-physics systems with two processes. While this limitation was implemented specifically for these experiments, it’s important to emphasize that our framework inherently supports systems with any number of processes. Throughout all experiments, we maintained constant coefficients and boundary conditions to isolate and analyze the impact of initial conditions on system evolution. The primary objective of our evaluation was to learn an effective mapping from the initial conditions ($t = 0$) to the final solutions after a specified number of time steps ($t = T$). By maintaining fixed coefficients and boundary conditions, we could thoroughly assess our framework’s ability to capture and model the complex dynamics and interactions between processes, focusing specifically on how variations in initial conditions influence the system’s evolution.

Competing Methods In our experimental evaluation, we examine three variants of our proposed framework, each employing distinct aggregation mechanisms. The primary variants include COMPOL-RNN, which utilizes a recurrent aggregation mechanism, and COMPOL-ATN, which implements an attention-based aggregation approach. To provide enhanced flexibility in modeling complex interactions, we introduce an additional variant, COMPOL-MH-ATN, which leverages multi-head attention for aggregation. This third variant extends the capabilities of the basic attention

mechanism by enabling the model to capture multiple types of relationships simultaneously through its multi-headed architecture Vaswani (2017).

We evaluated our framework against two leading neural operators for coupled multi-physics systems: FNO and CMWNO¹. FNO was adapted using process concatenation as input channels (FNO_c) to capture interactions in Fourier space, while CMWNO modeled inter-process dependencies through decoupled integral kernels in multiwavelet operations. For implementation consistency, all models were developed in PyTorch (Paszke et al., 2019) and trained using the Adam optimizer (Diederik, 2014) with a 0.001 learning rate and cosine annealing schedule for optimal convergence (Loshchilov and Hutter, 2016). The computations were performed on an NVIDIA RTX 4090 GPU with 24GB memory. To ensure robust evaluation, we employed 5-fold cross-validation, dividing the dataset into five equal segments. Each segment served as the validation set once while the remaining data was used for training. Performance was measured using averaged relative L_2 error on a separate test dataset, with standard deviations reported across all folds. Due to structural constraints, CMWNO comparisons were restricted to 1-D experiments only.

5.1 Benchmarks

1-D Lotka-Volterra Equation The 1-D reaction-diffusion Lotka-Volterra system models predator-prey population dynamics through coupled partial differential equations:

$$\begin{cases} \frac{\partial u}{\partial t} = D_u \nabla^2 u + au - buv \\ \frac{\partial v}{\partial t} = D_v \nabla^2 v + cuv - dv \end{cases}$$

The system combines spatial diffusion (coefficients D_u and D_v) with population interactions through reaction terms, generating complex spatio-temporal patterns. We study this system using a one-dimensional Gaussian Random Field initialization (length-scale $l = 0.1$, amplitude $\sigma = 0.5$) with periodic boundary conditions and uniform interaction parameters ($a = b = c = d = 0.01$) to examine the fundamental dynamics.

1-D Coupled Burgers' Equation The coupled Burgers' equation models the evolution of two interrelated spatio-temporal variables, $u(x, t)$ and $v(x, t)$, through a pair of interconnected equations:

$$\begin{cases} \frac{\partial u}{\partial t} = -u \frac{\partial u}{\partial x} - v \frac{\partial u}{\partial x} + \nu \nabla^2 u \\ \frac{\partial v}{\partial t} = -v \frac{\partial v}{\partial x} - u \frac{\partial v}{\partial x} + \nu \nabla^2 v \end{cases}$$

The system's behavior is governed by the viscosity coefficient ν , which controls diffusion strength. The equations are coupled through advection terms $v \frac{\partial u}{\partial x}$ and $u \frac{\partial v}{\partial x}$, enabling the system to model fluid interactions, wave propagation, and transport processes in multi-component systems. At low viscosity values ($\nu = 0.1$ in our setup), the nonlinear advection terms become dominant, potentially producing shock waves. Using Gaussian pulse initial conditions with Dirichlet boundary conditions, we aimed to map these initial states to system solutions at time $T = 2$.

2-D Grey-Scott Equation The Gray-Scott equations model pattern formation in chemical reactions through coupled partial differential equations:

$$\begin{cases} \frac{\partial u}{\partial t} = D_u \nabla^2 u - uv^2 + F(1 - u) \\ \frac{\partial v}{\partial t} = D_v \nabla^2 v + uv^2 + (F + k)v \end{cases}$$

1. <https://github.com/joshuaxiao98/CMWNO>

The system tracks two chemical species: an activator (u) and an inhibitor (v). Their evolution is governed by diffusion (coefficients D_u and D_v), an autocatalytic reaction (uv^2), and regulatory mechanisms through feeding rate F and removal rate k . The interplay of these processes generates diverse patterns like spots and stripes, with their characteristics determined by the system parameters. To study these pattern-forming dynamics, we examine the system’s evolution from a two-dimensional Gaussian Random Field initial condition to time $T = 20$, observing how perturbations develop into organized spatial structures. For all experiments reported in Tables 1 and 2, we employed the Gray-Scott system parameters $D_u = 0.12$, $D_v = 0.06$, $F = 0.054$, and $k = 0.063$.

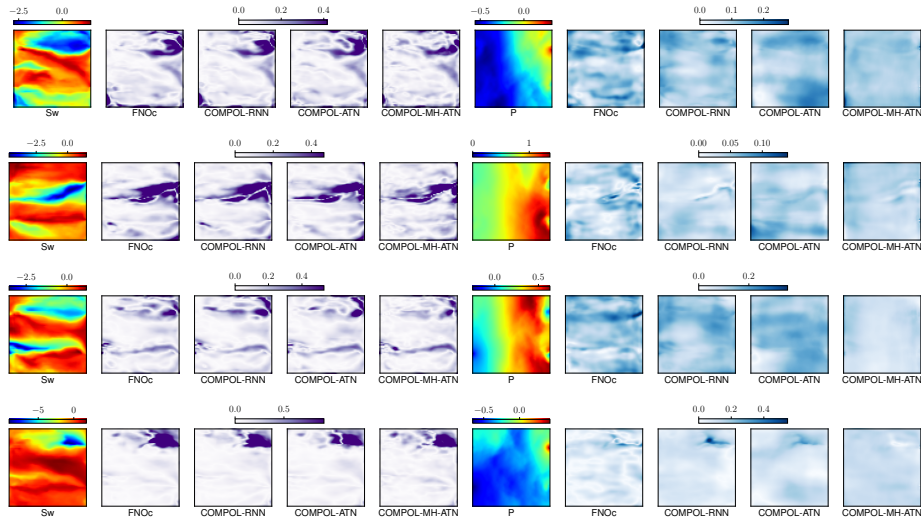


Figure 2: Visualization of element-wise solution errors of *Multiphase Flow* at $n_{\text{train}} = 256$. The first and sixth columns show the ground-truth values of water phase saturation and water phase pressure, respectively. The remaining columns display the absolute errors for each comparative method, where lighter colors indicate smaller errors.

Multiphase Flow Multiphase flow describes fluid mixtures moving simultaneously—a process critical for underground resource management, including oil and gas extraction, geological carbon storage, and nuclear waste disposal. We study oil-water two-phase flow using GEOS² on a 2D domain with water injection and oil extraction points on opposite boundaries. The domain permeability ranges from $1mD$ to $1000mD$, sampled based on the fractal distribution (Tang et al., 2021). Our dataset includes 1024 scenarios with varying boundary configurations, each simulated for 15 timesteps over 7.5×10^6 seconds. The goal is to predict the evolution of phase pressure (P_p) and saturation (S_p) distributions. Section A provides detailed specifications.

5.2 Performance Analysis

Our experimental evaluation demonstrates the superior performance of our proposed model across four benchmark problems, using a limited training dataset of 256 examples. Table 1 presents the relative L_2 errors on test data, averaged across five different training data folds with accompanying standard deviations. The results reveal significant performance improvements compared to existing

2. <https://github.com/GEOS-DEV/GEOS>

methods. Specifically, our model outperforms both FNO and CMWNO by substantial margins: approximately 55% reduction in error for the Lotka-Volterra and Gray-Scott systems, 80% improvement for the Coupled Burgers equation, and 33% enhancement for the Multiphase Flow problem. To validate these findings, we conducted additional experiments with an expanded training set of 512 examples, reported in Table 2 in section B.1. These results consistently support our initial observations regarding the model’s superior performance. To establish the model’s robustness, we conducted extensive parameter sensitivity analyses. This included systematic variation of initial conditions through different length-scales and amplitudes of the Gaussian random field, with comprehensive results detailed in section B.2. For the Gray-Scott equation specifically, we performed additional testing across varied feeding and removal rates, documented in section B.3. These sensitivity studies consistently demonstrated our method’s superior performance through comparative analysis of relative L_2 errors. The quantitative improvements are further supported by qualitative visual evidence. Error field visualizations are presented in Figure 2 for the Multiphase Flow problem and Figure 3 in section B.4 for the Gray-Scott system, providing clear visual confirmation of our model’s enhanced prediction accuracy. These visualizations effectively illustrate the practical significance of the performance improvements achieved by our approach.

6. Conclusion

We have introduced COMPOL, a novel coupled multi-physics neural operator learning framework that extends Fourier neural operators to effectively model interactions between multiple physical processes in complex systems. Our approach employs innovative feature aggregation techniques using recurrent and attention mechanisms to capture rich interdependencies in the latent space. Extensive experiments demonstrate that COMPOL achieves significant improvements in predictive accuracy compared to state-of-the-art methods. These results highlight the effectiveness of our feature aggregation approach for learning the complex dynamics of coupled multi-physics systems.

References

- Jamal Hussein Abou-Kassem, Syed Mohammad Farouq-Ali, and M Rafiq Islam. Petroleum Reservoir Simulations. Elsevier, 2013.
- Vladimir Igorevich Arnol’d. Mathematical methods of classical mechanics, volume 60. Springer Science & Business Media, 2013.
- Dzmitry Bahdanau. Neural machine translation by jointly learning to align and translate. arXiv preprint arXiv:1409.0473, 2014.
- Yuri Bazilevs, Kenji Takizawa, and Tayfun E Tezduyar. Computational fluid-structure interaction: methods and applications. John Wiley & Sons, 2013.
- Jacob Bear and Alexander H-D Cheng. Modeling groundwater flow and contaminant transport, volume 23. Springer, 2010.
- Yoshua Bengio, Patrice Simard, and Paolo Frasconi. Learning long-term dependencies with gradient descent is difficult. IEEE transactions on neural networks, 5(2):157–166, 1994.
- Theodore L Bergman. Fundamentals of heat and mass transfer. John Wiley & Sons, 2011.

- Oussama Boussif, Yoshua Bengio, Loubna Benabbou, and Dan Assouline. Magnet: Mesh agnostic neural pde solver. Advances in Neural Information Processing Systems, 35:31972–31985, 2022.
- H Brezis. Functional analysis, sobolev spaces and partial differential equations, 2011.
- Hans-Joachim Bungartz and Michael Schäfer. Fluid-structure interaction: modelling, simulation, optimisation, volume 53. Springer Science & Business Media, 2006.
- Peter Yichen Chen, Jinxu Xiang, Dong Heon Cho, Yue Chang, GA Pershing, Henrique Teles Maia, Maurizio M Chiaramonte, Kevin Carlberg, and Eitan Grinspun. Crom: Continuous reduced-order modeling of pdes using implicit neural representations. arXiv preprint arXiv:2206.02607, 2022.
- Kyunghyun Cho, Bart Van Merriënboer, Caglar Gulcehre, Dzmitry Bahdanau, Fethi Bougares, Holger Schwenk, and Yoshua Bengio. Learning phrase representations using rnn encoder-decoder for statistical machine translation. arXiv preprint arXiv:1406.1078, 2014.
- Alexandre Joel Chorin, Jerrold E Marsden, and Jerrold E Marsden. A mathematical introduction to fluid mechanics, volume 3. Springer, 1990.
- Stefano Conti and Anthony O’Hagan. Bayesian emulation of complex multi-output and dynamic computer models. Journal of statistical planning and inference, 140(3):640–651, 2010.
- James W Cooley and John W Tukey. An algorithm for the machine calculation of complex fourier series. Mathematics of computation, 19(90):297–301, 1965.
- Michael Cross and Henry Greenside. Pattern formation and dynamics in nonequilibrium systems. Cambridge University Press, 2009.
- P Kingma Diederik. Adam: A method for stochastic optimization. (No Title), 2014.
- Jeffrey L Elman. Finding structure in time. Cognitive science, 14(2):179–211, 1990.
- Soheil Esmailzadeh, Kamyar Azizzadenesheli, Karthik Kashinath, Mustafa Mustafa, Hamdi A Tchelepi, Philip Marcus, Mr Prabhat, Anima Anandkumar, et al. Meshfreeflownet: A physics-constrained deep continuous space-time super-resolution framework. In SC20: International Conference for High Performance Computing, Networking, Storage and Analysis, pages 1–15. IEEE, 2020.
- Lawrence C Evans. Partial differential equations, volume 19. American Mathematical Society, 2022.
- Carlos A Felippa, Kwang-Chun Park, and Charbel Farhat. Partitioned analysis of coupled mechanical systems. Computer methods in applied mechanics and engineering, 190(24-25):3247–3270, 2001.
- Alex Graves. Neural turing machines. arXiv preprint arXiv:1410.5401, 2014.
- Alex Graves and Alex Graves. Long short-term memory. Supervised sequence labelling with recurrent neural networks, pages 37–45, 2012.
- Peter Grindrod. The theory and applications of reaction-diffusion equations: patterns and waves. (No Title), 1996.

- Gaurav Gupta, Xiongye Xiao, and Paul Bogdan. Multiwavelet-based operator learning for differential equations. Advances in neural information processing systems, 34:24048–24062, 2021.
- Zhongkai Hao, Chang Su, Songming Liu, Julius Berner, Chengyang Ying, Hang Su, Anima Anandkumar, Jian Song, and Jun Zhu. Dpot: Auto-regressive denoising operator transformer for large-scale pde pre-training. arXiv preprint arXiv:2403.03542, 2024.
- Leila Hashemi, Martin Blunt, and Hadi Hajibeygi. Pore-scale modelling and sensitivity analyses of hydrogen-brine multiphase flow in geological porous media. Scientific reports, 11(1):8348, 2021.
- Dave Higdon, James Gattiker, Brian Williams, and Maria Rightley. Computer model calibration using high-dimensional output. Journal of the American Statistical Association, 103(482):570–583, 2008.
- Philip Holmes. Turbulence, coherent structures, dynamical systems and symmetry. Cambridge university press, 2012.
- Zhe Hu, Wenyong Tang, Hongxiang Xue, and Xiaoying Zhang. A simple-based monolithic implicit method for strong-coupled fluid–structure interaction problems with free surfaces. Computer Methods in Applied Mechanics and Engineering, 299:90–115, 2016.
- Thomas JR Hughes. The finite element method: linear static and dynamic finite element analysis. Courier Corporation, 2003.
- Rafal Jozefowicz, Wojciech Zaremba, and Ilya Sutskever. An empirical exploration of recurrent network architectures. In International conference on machine learning, pages 2342–2350. PMLR, 2015.
- Leonid Vitalevich Kantorovich and Gleb Pavlovich Akilov. Functional analysis. Elsevier, 2014.
- Marc C Kennedy and Anthony O’Hagan. Predicting the output from a complex computer code when fast approximations are available. Biometrika, 87(1):1–13, 2000.
- David E Keyes, Lois C McInnes, Carol Woodward, William Gropp, Eric Myra, Michael Pernice, John Bell, Jed Brown, Alain Clo, Jeffrey Connors, et al. Multiphysics simulations: Challenges and opportunities. The International Journal of High Performance Computing Applications, 27(1):4–83, 2013.
- Nikola Kovachki, Zongyi Li, Burigede Liu, Kamyar Azizzadenesheli, Kaushik Bhattacharya, Andrew Stuart, and Anima Anandkumar. Neural operator: Learning maps between function spaces with applications to pdes. Journal of Machine Learning Research, 24(89):1–97, 2023.
- Stig Larsson and Vidar Thomée. Partial differential equations with numerical methods, volume 45. Springer, 2003.
- Randall J LeVeque. Finite difference methods for ordinary and partial differential equations: steady-state and time-dependent problems. SIAM, 2007.
- Shibo Li, Wei Xing, Robert M Kirby, and Shandian Zhe. Scalable gaussian process regression networks. In Proceedings of the Twenty-Ninth International Conference on International Joint Conferences on Artificial Intelligence, pages 2456–2462, 2021.

- Shibo Li, Zheng Wang, Robert Kirby, and Shandian Zhe. Infinite-fidelity coregionalization for physical simulation. Advances in Neural Information Processing Systems, 35:25965–25978, 2022a.
- Shibo Li, Zheng Wang, Robert Kirby, and Shandian Zhe. Deep multi-fidelity active learning of high-dimensional outputs. In The 25th International Conference on Artificial Intelligence and Statistics, 2022b.
- Shibo Li, Li Shi, and Shandian Zhe. Infinite-fidelity surrogate learning via high-order gaussian processes. In The 1st Synergy of Scientific and Machine Learning Modelling Workshop @ ICML, 2023.
- Shibo Li, Xin Yu, Wei Xing, Mike Kirby, Akil Narayan, and Shandian Zhe. Multi-resolution active learning of fourier neural operators. In The 27th International Conference on Artificial Intelligence and Statistics (AISTATS), 2024.
- Zongyi Li, Nikola Kovachki, Kamyar Azizzadenesheli, Burigede Liu, Kaushik Bhattacharya, Andrew Stuart, and Anima Anandkumar. Fourier neural operator for parametric partial differential equations. arXiv preprint arXiv:2010.08895, 2020a.
- Zongyi Li, Nikola Kovachki, Kamyar Azizzadenesheli, Burigede Liu, Kaushik Bhattacharya, Andrew Stuart, and Anima Anandkumar. Neural operator: Graph kernel network for partial differential equations. arXiv preprint arXiv:2003.03485, 2020b.
- Zongyi Li, Nikola Kovachki, Kamyar Azizzadenesheli, Burigede Liu, Andrew Stuart, Kaushik Bhattacharya, and Anima Anandkumar. Multipole graph neural operator for parametric partial differential equations. Advances in Neural Information Processing Systems, 33:6755–6766, 2020c.
- Ilya Loshchilov and Frank Hutter. Sgdr: Stochastic gradient descent with warm restarts. arXiv preprint arXiv:1608.03983, 2016.
- Lu Lu, Pengzhan Jin, Guofei Pang, Zhongqiang Zhang, and George Em Karniadakis. Learning nonlinear operators via deeponet based on the universal approximation theorem of operators. Nature machine intelligence, 3(3):218–229, 2021.
- Lu Lu, Xuhui Meng, Shengze Cai, Zhiping Mao, Somdatta Goswami, Zhongqiang Zhang, and George Em Karniadakis. A comprehensive and fair comparison of two neural operators (with practical extensions) based on fair data. Computer Methods in Applied Mechanics and Engineering, 393:114778, 2022.
- Michael McCabe, Bruno Régaldo-Saint Blancard, Liam Holden Parker, Ruben Ohana, Miles Cranmer, Alberto Bietti, Michael Eickenberg, Siavash Golkar, Geraud Krawezik, Francois Lanusse, et al. Multiple physics pretraining for physical surrogate models. arXiv preprint arXiv:2310.02994, 2023.
- James D Murray. Mathematical biology: I. An introduction, volume 17. Springer Science & Business Media, 2007.

- J Tinsley Oden and Serge Prudhomme. Estimation of modeling error in computational mechanics. Journal of Computational Physics, 182(2):496–515, 2002.
- R Pascanu. How to construct deep recurrent neural networks. arXiv preprint arXiv:1312.6026, 2013.
- Adam Paszke, Sam Gross, Francisco Massa, Adam Lerer, James Bradbury, Gregory Chanan, Trevor Killeen, Zeming Lin, Natalia Gimelshein, Luca Antiga, et al. Pytorch: An imperative style, high-performance deep learning library. Advances in neural information processing systems, 32, 2019.
- John E Pearson. Complex patterns in a simple system. Science, 261(5118):189–192, 1993.
- Pourya Pilva and Ahmad Zareei. Learning time-dependent pde solver using message passing graph neural networks. arXiv preprint arXiv:2204.07651, 2022.
- Alfio Quarteroni and Silvia Quarteroni. Numerical models for differential problems, volume 2. Springer, 2009.
- Alfio Quarteroni and Alberto Valli. Numerical approximation of partial differential equations, volume 23. Springer Science & Business Media, 2008.
- Alfio Quarteroni, Riccardo Sacco, and Fausto Saleri. Numerical mathematics, volume 37. Springer Science & Business Media, 2010.
- Md Ashiqur Rahman, Robert Joseph George, Mogab Elleithy, Daniel Leibovici, Zongyi Li, Boris Boney, Colin White, Julius Berner, Raymond A Yeh, Jean Kossaifi, et al. Pretraining codomain attention neural operators for solving multiphysics pdes. arXiv preprint arXiv:2403.12553, 2024.
- Maziar Raissi, Paris Perdikaris, and George E Karniadakis. Physics-informed neural networks: A deep learning framework for solving forward and inverse problems involving nonlinear partial differential equations. Journal of Computational physics, 378:686–707, 2019.
- Michael Reed and Barry Simon. Methods of modern mathematical physics: Functional analysis, volume 1. Gulf Professional Publishing, 1980.
- Elias M Stein and Rami Shakarchi. Fourier analysis: an introduction, volume 1. Princeton University Press, 2011.
- C Susanne, L Brenner, and LR Scott. The mathematical theory of finite element methods. Texts in Applied Mathematics, 15, 1994.
- Hwei Tang, Pengcheng Fu, Jize Sherman, Christopher S. and Zhang, Xin Ju, Francois Hamon, Nicholas A. Azzolina, Matthew Burton-Kelly, and Joseph P. Morris. A deep learning-accelerated data assimilation and forecasting workflow for commercial-scale geologic carbon storage. International Journal of Greenhouse Gas Control, 22, 2021.
- Hwei Tang, Qingkai Kong, and Joseph Morris. Large-scale geological carbon storage modeling with multi-fidelity fourier neural operator. In AGU Fall Meeting Abstracts, volume 2023, pages H31I–02, 2023.

- Hewei Tang, Qingkai Kong, and Joseph P Morris. Multi-fidelity fourier neural operator for fast modeling of large-scale geological carbon storage. Journal of Hydrology, 629:130641, 2024.
- A Vaswani. Attention is all you need. Advances in Neural Information Processing Systems, 2017.
- Zheng Wang, Wei Xing, Robert Kirby, and Shandian Zhe. Multi-fidelity high-order gaussian processes for physical simulation. In International Conference on Artificial Intelligence and Statistics, pages 847–855. PMLR, 2021.
- E Weinan and Bjorn Engquist. Multiscale modeling and computation. Notices of the AMS, 50(9): 1062–1070, 2003.
- Gege Wen, Zongyi Li, Kamyar Azizzadenesheli, Anima Anandkumar, and Sally M Benson. U-fno—an enhanced fourier neural operator-based deep-learning model for multiphase flow. Advances in Water Resources, 163:104180, 2022.
- Paul J Werbos. Backpropagation through time: what it does and how to do it. Proceedings of the IEEE, 78(10):1550–1560, 1990.
- Xiongye Xiao, Defu Cao, Ruochen Yang, Gaurav Gupta, Gengshuo Liu, Chenzhong Yin, Radu Balan, and Paul Bogdan. Coupled multiwavelet neural operator learning for coupled partial differential equations. arXiv preprint arXiv:2303.02304, 2023.
- Wei W Xing, Robert M Kirby, and Shandian Zhe. Deep coregionalization for the emulation of simulation-based spatial-temporal fields. Journal of Computational Physics, 428:109984, 2021a.
- Wei W Xing, Akeel A Shah, Peng Wang, Shandian Zhe, Qian Fu, and Robert M Kirby. Residual gaussian process: A tractable nonparametric bayesian emulator for multi-fidelity simulations. Applied Mathematical Modelling, 97:36–56, 2021b.
- Yuan Yin, Matthieu Kirchmeyer, Jean-Yves Franceschi, Alain Rakotomamonjy, and Patrick Gallinari. Continuous pde dynamics forecasting with implicit neural representations. arXiv preprint arXiv:2209.14855, 2022.
- Shandian Zhe, Wei Xing, and Robert M Kirby. Scalable high-order gaussian process regression. In The 22nd International Conference on Artificial Intelligence and Statistics, pages 2611–2620, 2019.

Appendix A. Details of Multiphase Flow

Multiphase flow is the simultaneous movement of two or more phases which is one of the most dominant subsurface processes for oil and gas extraction, transport of pollutants in subsurface environments, and geological carbon storage. Due to the presence of multiple phases, considerable complications are always encountered in describing and quantifying the nature of the flow. Here we present a 2D multiphase case of an underground oil-water two-phase flow. The components α (water) and β (oil) of the multiphase flow fulfill the mass conservation equation:

$$\begin{cases} \frac{\partial M^\alpha}{\partial t} = -\nabla \cdot (\mathbf{F}_a^\alpha + \mathbf{F}_d^\alpha) + q^\alpha \\ \frac{\partial M^\beta}{\partial t} = -\nabla \cdot (\mathbf{F}_a^\beta + \mathbf{F}_d^\beta) + q^\beta \end{cases}$$

where \mathbf{F}_a^α and \mathbf{F}_a^β are the advective mass flux, \mathbf{F}_d^α and \mathbf{F}_d^β are the diffusive mass flux, q^α and q^β are the source or sink terms, and M^α and M^β are the mass accumulation terms given by

$$\begin{cases} M^\alpha = \phi \sum_p S_p \rho_p X_p^\alpha \\ M^\beta = \phi \sum_p S_p \rho_p X_p^\beta \end{cases}$$

In the mass accumulation terms, ϕ is the porosity, S_p is the saturation of phase p , X_p^α or X_p^β is the mass fraction of component α or β in phase p , and ρ_p is the density of phase p . In the scenarios of subsurface oil-water two-phase flow, \mathbf{F}_d^α and \mathbf{F}_d^β including molecular diffusion and hydrodynamic dispersion are often negligible when compared to \mathbf{F}_a^α and \mathbf{F}_a^β . For simplicity, we don't include diffusion terms in our simulations. And the advective mass flux equations of component α and β are

$$\begin{cases} \mathbf{F}_a^\alpha|_a = \sum_p X_p^\alpha \rho_p \mathbf{u}_p \\ \mathbf{F}_a^\beta|_a = \sum_p X_p^\beta \rho_p \mathbf{u}_p \end{cases}$$

Here, \mathbf{u}_p is the Darcy velocity of phase p defined as follows:

$$\mathbf{u}_p = -k (\nabla P_p - \rho_p \mathbf{g}) k_{rp} / \mu_p$$

where k is the absolute permeability tensor, P_p is the fluid pressure of phase p , \mathbf{g} is the gravitational acceleration, k_{rp} is the relative permeability of phase p , and μ_p is the viscosity of phase p . The fluid pressure for wetting phase P_w or non-wetting phase P_n is

$$P_n = P_w + P_c$$

where P_c is the capillary pressure.

In this study, the simulation is performed on GEOS which is an open-source multiphysics simulator. To simulate the oil-water two-phase flow, water is injected into a 2D (64×64 grids) domain from two randomly placed sources on the left boundary. And at the same, oil is produced from two randomly placed sinks on the right boundary. The permeability fields ($k_x=k_y$) are generated using a fractal algorithm with $k_{min} = 1mD$, $k_{max} = 1000mD$, and $k_{base} = 100mD$. And the porosity field is generated by the following correlation:

$$\phi = \left(\frac{k_x}{1 \times 10^{-15} \times 0.0009} \right)^{\frac{1}{4.0001}} \times \frac{1}{100}$$

For the 1024 cases in the dataset, we keep all other conditions identical and only change the locations of sources and sinks. For each case, the multiphysics solver is performed every 5×10^5 seconds for 15 times and the whole simulation has a time duration of 7.5×10^6 . During the simulation, the spatial and temporal results of phase pressure and phase saturation are stored at every time step which makes the dimension of the dataset to be $1024 \times 15 \times 64 \times 64 \times 2$. Our objective here is to learn the mapping from an earlier spatial distribution of S_p and P_p to that of a later time step.

Appendix B. Prediction Accuracy Results

B.1 Additional Relative L_2 Error Across Benchmark Tests

Method	<i>Lotka-Volterra</i>	<i>Coupled-Burgers</i>	<i>Grey-Scott</i>	<i>Multiphase Flow</i>
FNO_c	0.1719 ± 0.0091	$1.973e-4 \pm 5.527e-6$	0.0040 ± 0.0001	0.0125 ± 0.0015
CMWNO	0.1729 ± 0.0241	0.0301 ± 0.0007	-	-
COMPOL-RNN	0.0801 ± 0.0038	$2.061e-5 \pm 6.435e-7$	$0.0028 \pm 5.9e-5$	0.0104 ± 0.0023
COMPOL-ATN	0.0740 ± 0.0023	$5.986e-5 \pm 1.903e-6$	$0.0034 \pm 5.8e-5$	$0.0098 \pm 2.3e-4$
COMPOL-MH-ATN	0.0747 ± 0.0021	$6.047e-5 \pm 2.384e-6$	0.0031 ± 0.0009	$0.0077 \pm 5.5e-4$

Table 2: Prediction accuracy evaluated using relative L_2 error on four benchmark datasets with 512 training examples. Results show averages from five independent runs to ensure statistical reliability.

B.2 Expanded Results for Lotka-Volterra Under Diverse Initial Conditions

	ntrain = 256	ntrain = 512
FNO_c	0.3100 ± 0.0268	0.2206 ± 0.0131
CMWNO	0.3078 ± 0.0306	0.2243 ± 0.0303
COMPOL-RNN	0.1504 ± 0.0053	0.0943 ± 0.0032
COMPOL-ATN	0.1458 ± 0.0044	0.0903 ± 0.0020
COMPOL-MH-ATN	0.1474 ± 0.0059	0.0847 ± 0.0027

Table 3: Testing relative L_2 errors for input functions sampled from a Gaussian Random Field (GRF) with length scale $l = 0.1$ and amplitude $\sigma = 1.0$.

	ntrain = 256	ntrain = 512
FNO_c	0.0748 ± 0.0049	0.0508 ± 0.0035
CMWNO	0.1321 ± 0.0267	0.0903 ± 0.0207
COMPOL-RNN	0.0403 ± 0.0013	0.0213 ± 0.0014
COMPOL-ATN	0.0375 ± 0.0026	0.0218 ± 0.0012
COMPOL-MH-ATN	0.0385 ± 0.0018	0.0204 ± 0.0007

Table 4: Testing relative L_2 errors for input functions sampled from a Gaussian Random Field (GRF) with length scale $l = 0.2$ and amplitude $\sigma = 0.5$.

	ntrain = 256	ntrain = 512
FNO _c	0.1221 ± 0.0060	0.0806 ± 0.0032
CMWNO	0.2280 ± 0.0509	0.1616 ± 0.0639
COMPOL-RNN	0.0640 ± 0.0035	0.0514 ± 0.0026
COMPOL-ATN	0.0518 ± 0.0025	0.0394 ± 0.0024
COMPOL-MH-ATN	0.0559 ± 0.0038	0.0388 ± 0.0014

Table 5: Testing relative L_2 errors for input functions sampled from a Gaussian Random Field (GRF) with length scale $l = 0.2$ and amplitude $\sigma = 1.0$.

	ntrain = 256	ntrain = 512
FNO _c	0.0284 ± 0.0006	0.0205 ± 0.0011
CMWNO	0.1534 ± 0.0444	0.1006 ± 0.0497
COMPOL-RNN	0.0118 ± 0.0006	0.0079 ± 0.0003
COMPOL-ATN	0.0112 ± 0.0007	0.0069 ± 0.0006
COMPOL-MH-ATN	0.0141 ± 0.0010	0.0080 ± 0.0003

Table 6: Testing relative L_2 errors for input functions sampled from a Gaussian Random Field (GRF) with length scale $l = 0.5$ and amplitude $\sigma = 1.0$.

	ntrain = 256	ntrain = 512
FNO _c	0.0340 ± 0.0019	0.0221 ± 0.0020
CMWNO	0.0836 ± 0.0295	0.0562 ± 0.0189
COMPOL-RNN	0.0184 ± 0.0014	0.0133 ± 0.0029
COMPOL-ATN	0.0156 ± 0.0018	0.0128 ± 0.0025
COMPOL-MH-ATN	0.0192 ± 0.0019	0.0123 ± 0.0023

Table 7: Testing relative L_2 errors for input functions sampled from a Gaussian Random Field (GRF) with length scale $l = 0.5$ and amplitude $\sigma = 0.5$.

B.3 Expanded Results for Grey-Scott Under Diverse PDEs Parameters

	ntrain = 256	ntrain = 512
FNO _c	0.0131 ± 0.0006	0.0056 ± 0.0001
COMPOL-RNN	0.0064 ± 0.0002	0.0029 ± 3.1e-5
COMPOL-ATN	0.0092 ± 0.0003	0.0038 ± 9.1e-5
COMPOL-MH-ATN	0.0077 ± 0.0003	0.0041 ± 0.0016

Table 8: Testing relative L_2 errors for Grey-Scott equation with $Du = 0.16, Dv = 0.08F = 0.062, k = 0.061$

B.4 Prediction Error Visualization

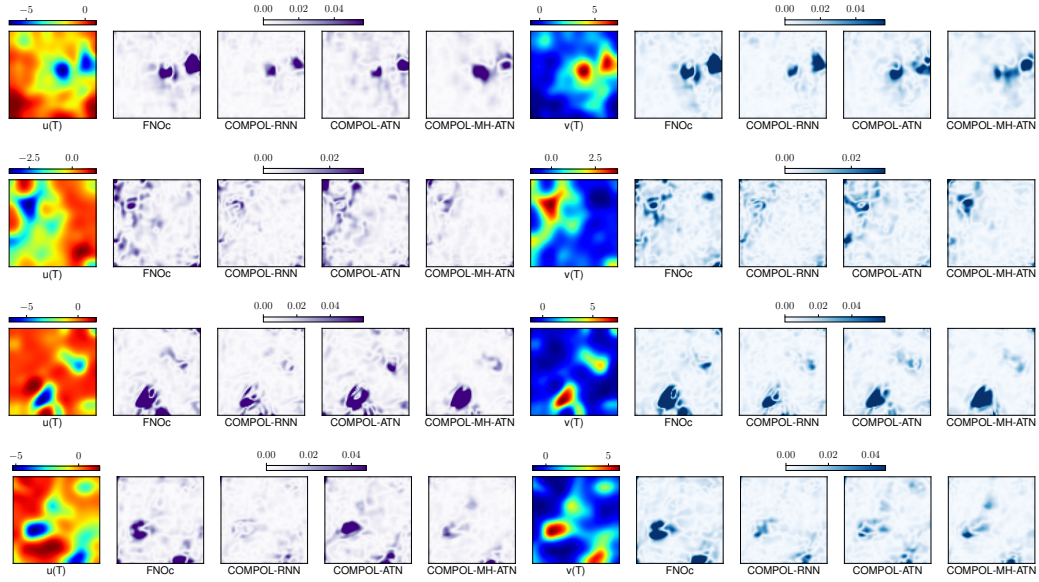


Figure 3: Visualization of element-wise solution errors of *Grey-Scott* at $n_{\text{train}} = 256$. The first and sixth columns show the ground-truth values of $u(T)$ and $v(T)$, respectively. The remaining columns display the absolute errors for each comparative method, where lighter colors indicate smaller errors.